

# ISTTOK Plasma Tomography Using Minimum Fisher Regularization

Daniel Hachmeister Ferreira da Costa  
daniel.hachmeister@tecnico.ulisboa.pt

Instituto Superior Técnico, Lisboa, Portugal

November 2019

## Abstract

A plasma tomography algorithm was developed for the ISTTOK tokamak. The algorithm is an instance of the Minimum Fisher Regularization, and was implemented and distributed as a *python* package. Plasma tomography is an ill-conditioned inversion problem. Reconstruction algorithms try to overcome this issue by introducing some form of *a priori* knowledge that requires empirical tuning. In general, to validate the implementation of these algorithms, either artificial phantoms are used, or one must rely on information provided by other diagnostics. In this work, an experimental setup was developed that allows the use of physical phantoms to tune and validate the reconstruction algorithm used. This also allowed the comparison of two different implementations of the algorithm regarding the mathematical description of the spatial sampling. A possible application of the tomographic diagnostic is demonstrated by computing the plasma position and observing the Shafranov shift.

**Keywords:** Plasma Tomography, Minimum Fisher, Tikhonov Regularization, Tokamak, Plasma Diagnostics

## 1. Introduction

Plasma tomography is a technique used to reconstruct the spatial distribution of a cross-sectional plasma profile from its line integrated measurements [1]. Here, we focus on the plasma radiation profile, which is reconstructed from plasma emissivity measurements. The reconstructed images (or tomograms) are obtained by sampling the plasma along lines of sight with arrays of optical sensors, such as pinhole cameras. One way of stating the tomography problem is with the matrix equation:

$$\mathbf{f} = \mathbf{T} \cdot \mathbf{g} \quad (1)$$

where  $\mathbf{f}$  represents the set of measurements from the various sensors,  $\mathbf{g}$  is the emissivity function represented on some orthogonal basis, usually a rectangular pixel grid, and  $\mathbf{T}$  is the so-called geometry matrix that describes how a given point in the emissivity profile  $\mathbf{g}$  contributes to the measurement of each sensor in  $\mathbf{f}$ .

The problem is ill-conditioned in nature, and to circumvent this problem some sort of regularization is needed. A common approach is to require smoothness of the reconstructed profile. The solution can be found by minimizing [2]:

$$\phi = \|\mathbf{T} \cdot \mathbf{g} - \mathbf{f}\|^2 + \alpha \|\mathbf{g}^T \cdot \mathbf{H} \cdot \mathbf{g}\|^2 \quad (2)$$

where the first term is the typical least-squares min-

imization ( $\chi^2$ ) and the second is the regularization term. Matrix  $\mathbf{H}$  represents the type of regularization to be imposed, and  $\alpha$  is the regularization parameter used to tune the strength of such regularization.

The correct implementation of a tomography algorithm depends on an accurate representation of the geometry matrix  $\mathbf{T}$ . The simplest implementation is based on a line of sight approach (LoS). The LoS matrix assumes that the pixels of the tomogram that contribute to the measurement of a given sensor lie along a straight line. This approximation is well motivated by the conservation of étendue [3]. However, a more complete description needs to take into account the full geometry of the pinhole and the sensors, which yields a volume of sight approach (VoS) [4].

Studies have been conducted to determine the performance of both the LoS and the VoS methods in a simulated environment, concluding that the VoS approach is recommended [4]. However, there is still a lack of experimental evidence.

## 2. Objectives

The goal of this work is to implement a tomography diagnostic for ISTTOK based on the currently available cameras. The algorithm of choice will be the Minimum Fisher Regularization (MFR), which

is perceived as one of the leading algorithms for plasma tomography in tokamaks [1].

Minimum Fisher Regularization works by imposing a strong smoothness where  $\mathbf{g}$  is small (low plasma emissivity), but allowing  $\mathbf{g}$  to be less smooth where it is large. It does so by minimizing the Fisher information defined in 1D as:

$$I_F = \int \frac{1}{g(x)} \left( \frac{\partial g(x)}{\partial x} \right)^2 dx \quad (3)$$

A demanding part of implementing a tomography diagnostic is its calibration and testing. Part of this work will thus be the calibration and validation of the diagnostic.

The importance of implementing a tomography diagnostic is that it unlocks the possibility of studying different research areas, namely:

- Detection of MHD modes with tomography - MHD modes are magnetic perturbations that should manifest in a deviation from the circular shape of the plasma cross-section [5].
- Study of impurity transport - sometimes heavy impurities are released from the tokamak wall onto the plasma. These manifest as a very bright but small localized source of light over the plasma background.
- Study of the plasma current inversion - Being one of the few tokamaks to have alternate current (AC) discharges, ISTTOK is the perfect test bench for studying how the plasma behaves during inversion, something that has only briefly been explored at the HT-7 tokamak [6].

### 3. Calibration & Testing

The ISTTOK tokamak has a circular cross-section with a major radius of 0.46 m and a minor radius of 8.5 cm at the limiter. The tomography diagnostic used in this work consists of two pinhole cameras toroidally aligned and positioned at poloidal angles  $0^\circ$  and  $90^\circ$ . Each camera contains a linear array of 16 photodiodes behind the pinhole, defining the lines of sight for each sensor. Figure 1 shows the cameras and the lines of sight. The photodiodes (AXUV20ELG by Opto Diode) have a spectral range from the soft X-rays to the infrared.<sup>1</sup> No optical filtering is used.

The system needs to be calibrated to determine the relative sensitivity (étendue) of each sensor. For this purpose, a negatoscope (or lightbox) was used as a uniform and isotropic light-emitting surface<sup>2</sup>.

<sup>1</sup>The photodiode array AXUV20ELG has 20 diodes of which we only use the middle 16 due to hardware constraints and limitations in the acquisition system.

<sup>2</sup>A negatoscope is a lightbox used to display x-ray films.

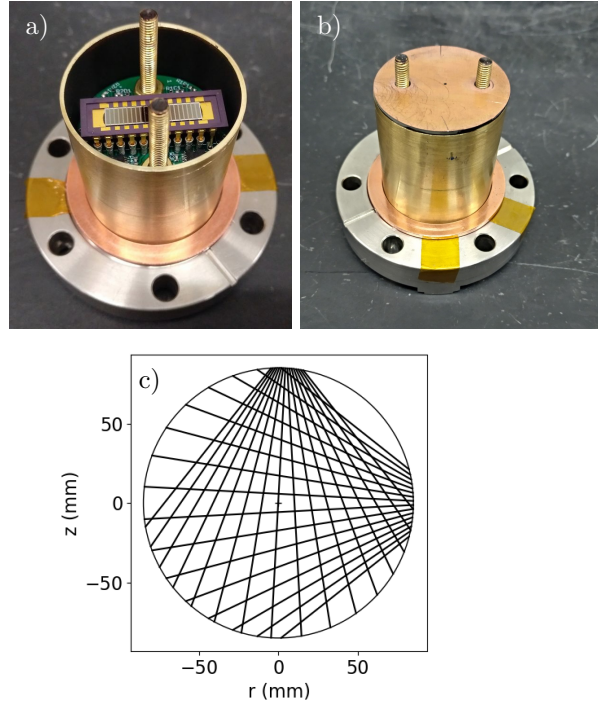


Figure 1: a) Camera without the pin-hole lid to show the photo-diode array; b) Camera with the pinhole lid; c) lines of sight for the cameras positioned at  $0^\circ$  and  $90^\circ$ .

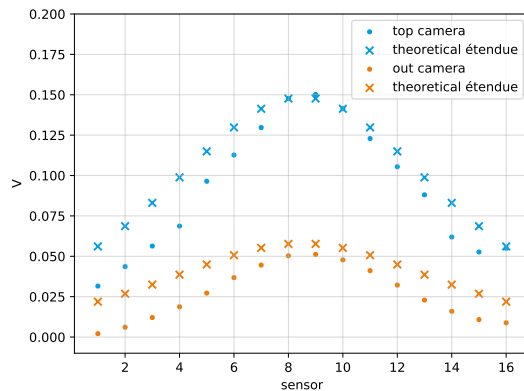


Figure 2: Voltage readings from the sensors versus the expected étendue for the outer and top cameras.

Figure 2 shows the measured signals with the cameras facing the calibration lightbox. The information retrieved from this calibration is then added to the geometry matrix  $\mathbf{T}$ .

As stated in the introduction, the calculation of the geometry matrix can be done either using the LoS or the VoS approaches.

The VoS matrix can be computed either using ray-tracing libraries [4], or by explicitly calculating the solid angle [7] for each sensor, which is the approach used for this work.

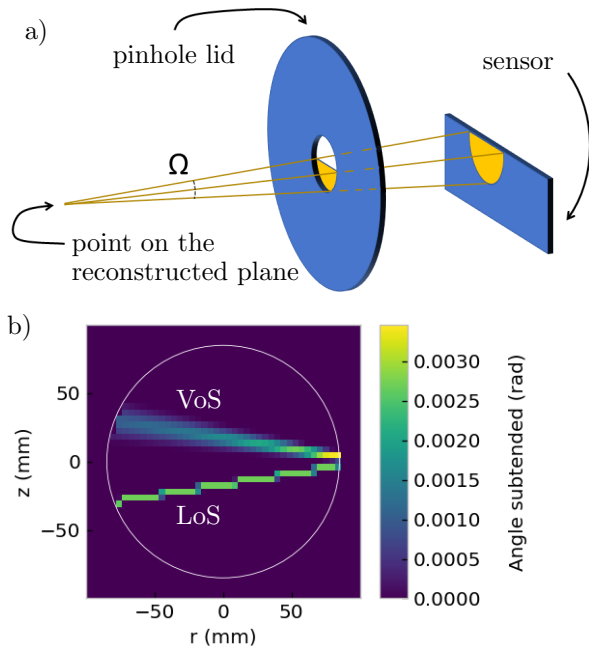


Figure 3: a) Example of the solid angle subtended by a pinhole setup; b) Individual pixel contributions to the measurement of a given sensor in both the VoS (top) and LoS (bottom) approximations.

Figure 3(a) shows the solid angle  $\Omega$  that needs to be computed at each point in space. This calculation assigns a certain weight to each pixel on the image plane proportional to  $\Omega$ .

In figure 3(b) we plot the values of the solid angle for each pixel. These values form a fading cone from the sensor. An equivalent LoS is also plotted for comparison.

To compare both approaches, a movable light source was used. The light source consisted of a cylindrical cold cathode lamp with a length of 50 mm and a diameter of 4 mm.

The lamp was held by a plastic structure inside a replica of the tokamak vessel, as shown in Figure 4(a). This structure allowed the placement of the source at different radial and angular positions. The lamp has an expected point-like emissivity for pixel sizes larger than its diameter. Knowing the expected emissivity profile, we can evaluate the quality of the reconstructions performed by the algorithm.

The pixel size used in this work was chosen to be the diameter of the lamp (around 4mm). At this resolution, the lamp is expected to act as a point source. The chosen pixel size also needed to be small enough to allow a clear distinction between the VoS and LoS matrices.

Given the expected emissivity  $\mathbf{g}$  of the lamp, we applied matrix  $\mathbf{T}$  to get the expected signals for the LoS and the VoS approaches. We then com-

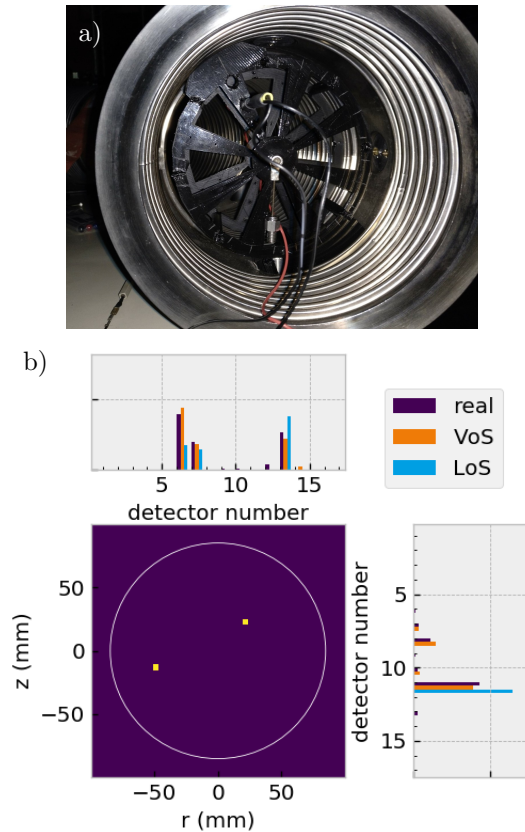


Figure 4: a) Cold cathode lamp and supporting structure inside the vessel replica; b) real vs. expected signals for the VoS and LoS geometries.

pared these results to the actual signals obtained from the experiment. Figure 4(b) shows an example of the real data versus the data predicted by the two  $\mathbf{T}$  matrices for two different lamp positions. The mean squared difference between expected and measured signals was 70% larger in the LoS case compared to the VoS case, evidence that the VoS matrix is indeed a more accurate representation of the setup geometry.

Reconstructions were performed with the acquired signals to determine the influence of each geometry matrix on the quality of the reconstructed profiles. To evaluate the resemblance between the reconstructed profile and the expected point-like emissivity, we computed the structural similarity index (SSIM) [8] between them. The VoS approach performed better in 50% of the cases, while the LoS performed better on 25% of the cases. The remaining 25% of the cases corresponded to an equal performance of both methods.

The better performance of the LoS approach was observed in instances where the lamp was aligned with a single sensor in each camera. In these cases, the algorithm yielded a sharp emissivity profile, which scored better than the somewhat more diffuse solution provided by the VoS approximation.

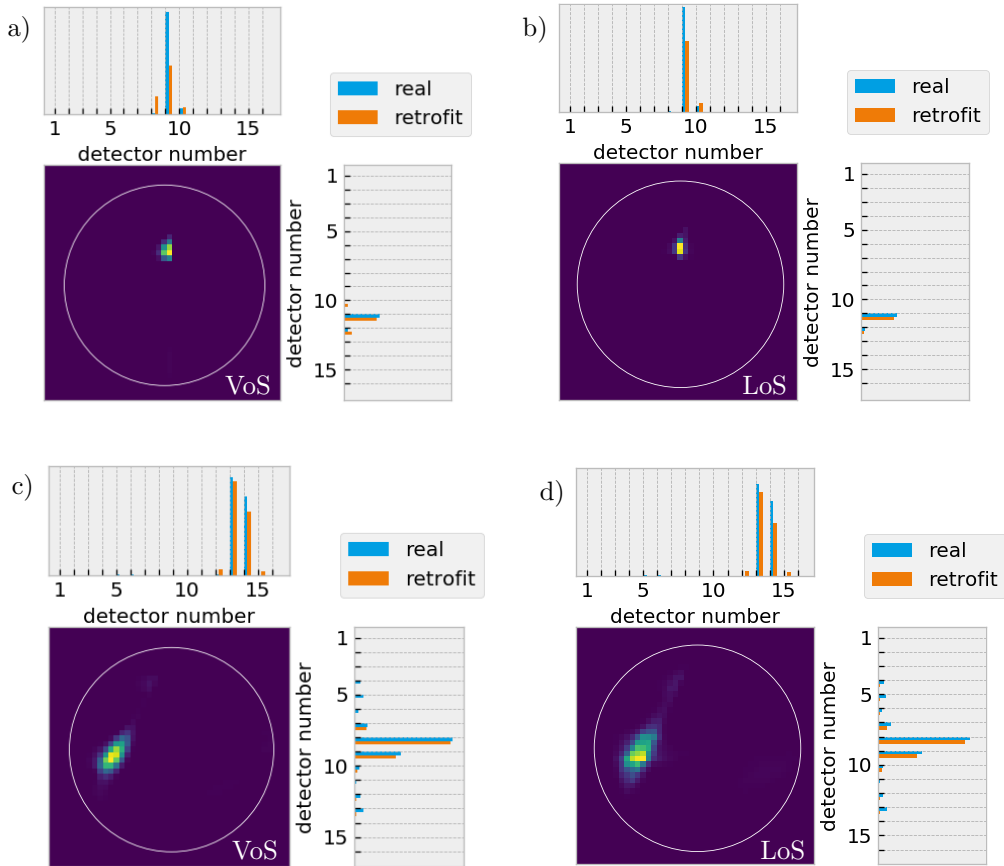


Figure 5: Single sensor illumination a) & b) vs. multiple sensor illumination c) & d) for the LoS and the VoS approximations. Bar plots show, for each camera, the signals measured by the detectors and the retrofit signals computed with eq. (1).

This is probably due to the larger area of the volumes of sight compared to the lines of sight.

Figures 5(a & b) show the reconstructions from an experiment with single sensor illumination. The LoS approach leads to a better reconstruction in the sense that it is closer to a point-like source. On the other hand, figures 5(c & d) show the results of multiple-sensor illumination. In this case, the LoS yields a broader profile because consecutive lines are further apart than consecutive volumes. In our case, consecutive volumes have a small overlap.

Finally, we compared both matrices by reconstructing a tomogram for a real shot.<sup>3</sup> Figure 6 shows the results of the reconstruction with both the VoS and LoS matrices. Both reconstructions were done with the same regularization constant  $\alpha$ . The LoS tomogram appears to be less smooth than the VoS one. In fact, referring to equation (2) the VoS tomogram has a regularization term  $\|\mathbf{g}^T \cdot \mathbf{H} \cdot \mathbf{g}\|^2$  that is 25 times smaller than

<sup>3</sup>Shot #45988 @309ms. Electron temperature at the core and electron density are respectively 150 eV and  $3 \times 10^{18} \text{m}^{-3}$ .

the same term in the LoS case, indicating that it is in fact more smooth. Meanwhile, both reconstructions have a similar  $\chi^2$ , with only a 15% difference. This suggests that there is an intrinsic regularization inherent to matrix  $\mathbf{T}$  in the VoS case, as would be expected by the broader nature of the volumes of sight.

#### 4. Applications

In this section, we give two example applications of the tomography diagnostic.

A straightforward application of the reconstructed plasma profile is using it to compute the position of the plasma centroid. Magnetic probes are commonly used to estimate the magnetic center of the plasma which is the center of the nested magnetic flux surfaces.

The plasma centroid computed through tomography is the center of mass of the emissivity profile which can be a useful variable for the control system. Because MFR is usually too slow for real-time applications, there is an interest in adaptations that can be faster [9]. We can bypass the reconstruction process and get a centroid estimate directly from

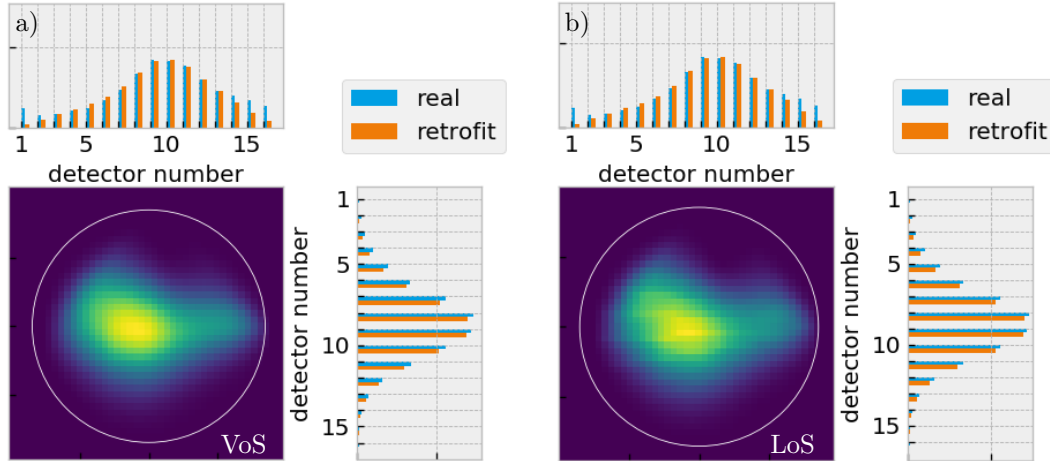


Figure 6: Plasma reconstructions made with a) volume of sight matrix and b) line of sight matrix. Bar plots show, for each camera, the signals measured by the detectors and the retrofit signals computed with eq. (1).

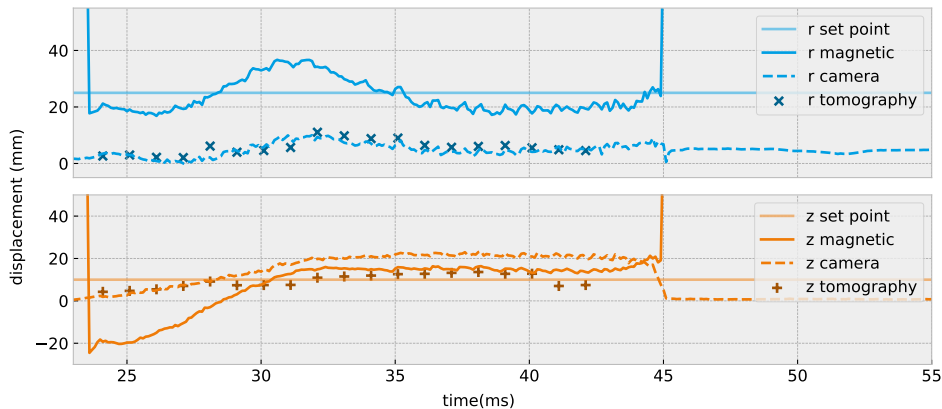


Figure 7: Plasma displacement in the horizontal (*top*) and vertical (*bottom*) directions.

the sensor measurements by finding an average line of sight on each camera and determining their intersection. The accuracy of this approximation needs to be verified using the output of the reconstruction algorithm.

Figure 7 compares the centroid estimates from both tomography and the magnetic diagnostic for shot #47220. The figure shows the horizontal displacement in the  $r$  coordinate and the vertical displacement in the  $z$  coordinate from the center of the vessel. The crosses represent the centroid estimate from the reconstructed profile and the dashed line represents the estimate from the average line of sight. For this shot, the setpoint for the magnetic center was ( $r = 2.5$ ,  $z = 1.0$ ). The correlation between the line of sight estimate and the magnetic diagnostic is 93% for the data shown in the figure.

There is a clear shift between the magnetic center and the emission center of mass, this shift is especially pronounced in the  $r$  displacement. The same

result has also been found in a similar analysis at the TCV [10] and at JET [2] where it has been suggested to arise from the Shafranov shift [11]. The Shafranov shift can be understood as an outward shift of the inner flux surfaces that makes them not concentric with the poloidal cross-section. Although the magnetic flux surfaces are displaced, this does not necessarily lead to a visible shift in the emissivity center of mass.

Another application of plasma tomography is in measuring magnetic instabilities or other types of magnetohydrodynamic (MHD) activity. The common approach to MHD analyses using tomography is through singular value decomposition (SVD) [13]. Although we do not use SVD for this work, we show that the current tomography set up can pick up the signal from MHD activity in the ISTTOK tokamak.

A common instability that can be observed in ISTTOK is a cylindrical rotating mode with  $m = 2$  and  $n = 1$  [14]. This rotating mode is illustrated

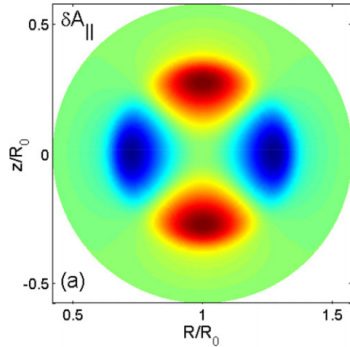


Figure 8: Fluctuations of the plasma toroidal current, responsible for generating the poloidal magnetic field. Taken from [12].

in figure 8. The figure shows a cross-sectional view of the plasma where we can see that the plasma current has two maxima and two minima. This gives rise to two maxima and minima of the poloidal magnetic field which can be easily picked up by the magnetic probes. These current fluctuations occur simultaneously as density fluctuations which means they can in principle be picked up by the tomography diagnostic.

Figure 9 shows the similarities between the spectrograms of the two signals. This indicates that these instabilities can be picked up by both the magnetic diagnostic and the tomography cameras. The rotating mode appears in the frequency spectrum as a bright spot between 50kHz – 80kHz.

Using the magnetic diagnostic, one can easily compute the angular position of the maxima and minima of the rotating mode as a function of time. Figure 10 shows the angular position of the maxima (in blue) and the minima (in red) as a function of time<sup>4</sup>. For any given instant, there are always two maxima 180° apart and two minima in between the maxima. This confirms that the mode has a poloidal number  $m = 2$ .

To perform a similar analysis using the tomography cameras we take the cross-correlation between sensors corresponding to different lines of sight. If the signals are in phase with each other it means they are both looking at maxima and minima at the same time. If they are in phase opposition it means that one is looking at a maximum while the other is looking at a minimum and vice-versa. Figure 11 shows the cross-correlation between LoS 1 and LoS 7 and 16 from the outer camera. LoS 1, 7, and 16 look respectively at the bottom, middle, and top of the tokamak. While LoS 1 and 16 have similar phases, LoS 7 is roughly in phase opposition with

<sup>4</sup>The figure actually shows the cross-correlation between the magnetic probes depending on their angular position but for the present discussion, both interpretations are equivalent.

the former two. Thus allowing the conclusion that the poloidal mode number corresponds to  $m = 2$ .

## 5. Conclusions

A plasma tomography algorithm has been implemented and can now be used as a diagnostic tool for tokamak ISTTOK to provide insight into the physics of fusion related plasmas.

This work also re-affirmed the need for proper calibration of tomography cameras, since the real étendue of each sensor deviates from the theoretical prediction significantly. A light-box, commonly used to display radiographs, proved to be an ideal tool to perform a relative calibration between cameras. Nevertheless, an absolute calibration would be key to recover the emissivity of the plasma in terms of power per unit volume.

We can also conclude that, by taking into account the full geometry of the system (the volume of sight approach), the weight of the regularization can be decreased and that this results in the ability to reconstruct sharper features in the plasma profile.

The Minimum Fisher algorithm proved capable of reconstructing the sharp emissivity profile of a small light source used as a physical phantom, and the reconstructions were improved by adding the full geometric description to the reconstruction algorithm.

As a proof of concept, the reconstruction algorithm was used to compute the center of mass of the emissivity. The center of mass was computed from the tomograms and also directly estimated from the sensor measurements. The result was compared to the one output by the magnetic diagnostic and proved to be well correlated (93%), although it shows a significant shift that ought to be investigated.

Lastly, it was proven that the tomography diagnostic can pick up information regarding MHD activity, which opens the door for future research into this area at ISTTOK.

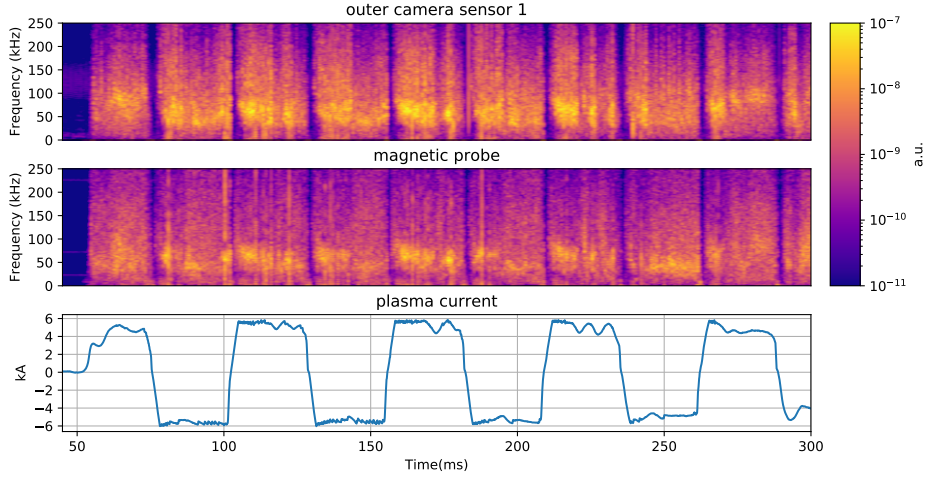


Figure 9: Spectrogram of the signal from the first sensor in the outer tomography camera (*top*), and for one of the magnetic probes (*middle*). Plasma current (*bottom*). Shot #47309.

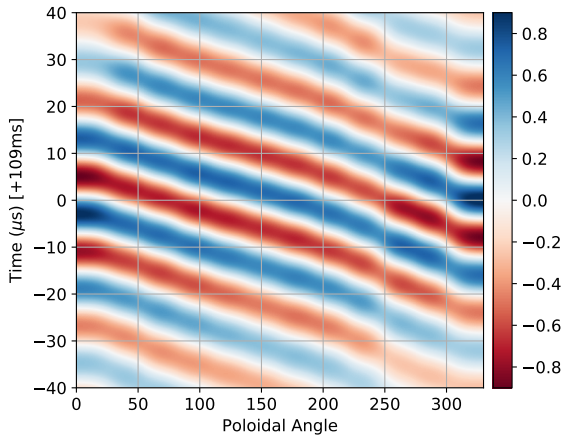


Figure 10: Angular position of the maxima and minima of the rotating mode, measured at 109ms for shot #47309.

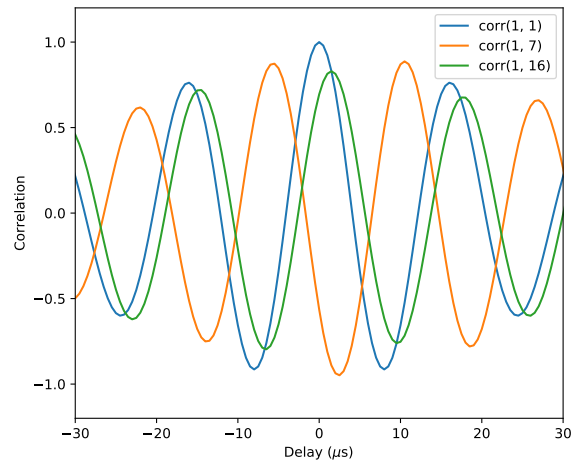


Figure 11: Cross correlation between the signals from LoS 1, 7, and 16 of the outer camera. Measured at 109ms for shot #47309.

## 6. Future Work

Having implemented and tested the diagnostic, the next step is naturally applying it to study plasma phenomena. Some of the possible applications are:

- Study of plasma position and comparison with the magnetic diagnostic.
- MHD mode analyses using singular value decomposition.
- Study of the plasma profile evolution during current inversion.

The Minimum Fisher Regularization was the algorithm of choice for this implementation. However, there are at least two other algorithms worth considering to extend the capabilities of the diagnostic. The Maximum Likelihood algorithm [15] and tomography using neural networks [16].

## References

- [1] Jan Mlynar, Teddy Craciunescu, Diogo R. Ferreira, Pedro Carvalho, Ondrej Ficker, Ondrej Grover, Martin Imrisek, Jakub Svoboda, and JET contributors. Current Research into Applications of Tomography for Fusion Diagnostics. *Journal of Fusion Energy*, 2018.
- [2] J. Mlynar, M. Imrisek, V. Weinzettl, M. Odstrcil, J. Havlicek, F. Janky, B. Alper, A. Murari, and JET-EFDA Contributors. Introducing minimum Fisher regularisation tomography to AXUV and soft x-ray diagnostic systems of the COMPASS tokamak. *Review of Scientific Instruments*, 2012.
- [3] M Anton, H Weisen, M J Dutch, W von der

- Linden, F Buhlmann, R Chavan, B Marletaz, P Marmillod, and P Paris. X-ray tomography on the TCV tokamak. *Plasma Physics and Controlled Fusion*, 1996.
- [4] M. Carr, A. Meakins, M. Bernert, P. David, C. Giroud, J. Harrison, S. Henderson, B. Lipschultz, F. Reimold, EUROfusion MST1 Team, and ASDEX Upgrade Team. Description of complex viewing geometries of fusion tomography diagnostics by ray-tracing. *Review of Scientific Instruments*, 2018.
- [5] O. Klüber, H. Zohm, H. Bruhns, J. Gernhardt, A. Kallenbach, and H. P. Zehrfeld. Mhd mode structure and propagation in the asdex tokamak. *Nuclear Fusion*, 1991.
- [6] Jiangang Li, Jiarong Luo, Shaojie Wang, Peng Fu, Biao Shen, Fukun Liu, Baonian Wan, Jiafang Shan, Guosheng Xu, Juan Huang, Jun Yu, Jiansheng Hu, Qiping Yuan, and Yeming Hu. Quasi-steady-state ac plasma current operation in HT-7 tokamak. *Nuclear Fusion*, 2007.
- [7] D. Vezinet, V. Igochine, M. Weiland, Q. Yu, A. Gude, D. Meshcheriakov, M. Sertoli, the Asdex Upgrade Team, and the EUROfusion MST1 Team. Non-monotonic growth rates of sawtooth precursors evidenced with a new method on ASDEX Upgrade. *Nuclear Fusion*, 2016.
- [8] Z. Wang, A.C. Bovik, H.R. Sheikh, and E.P. Simoncelli. Image Quality Assessment: From Error Visibility to Structural Similarity. *IEEE Transactions on Image Processing*, 2004.
- [9] J. Mlynar, V. Weinzettl, G. Bonheure, and A. Murari. Inversion techniques in the soft-X-ray tomography of fusion plasmas: Toward real-time applications. *Fusion Science and Technology*, 2010.
- [10] J Mlynar, S Coda, A Degeling, B P Duval, F Hofmann, T Goodman, J B Lister, X Llobet, and H Weisen. Investigation of the consistency of magnetic and soft x-ray plasma position measurements on TCV by means of a rapid tomographic inversion algorithm. *Plasma Physics and Controlled Fusion*, 2003.
- [11] I H Hutchinson. *Principles of Plasma Diagnostics*, chapter 2.2 Magnetohydrodynamic equilibrium. Cambridge University Press, second edition, 2002.
- [12] J. C. Li, C. J. Xiao, Z. H. Lin, and K. J. Wang. Effects of electron cyclotron current drive on magnetic islands in tokamak plasmas. *Physics of Plasmas*, 2017.
- [13] Dong Li, Yi Liu, J. Svensson, Y.Q. Liu, X.M. Song, L.M. Yu, Rui Mao, B.Z. Fu, Wei Deng, B.S. Yuan, X.Q. Ji, Yuan Xu, Wei Chen, Yan Zhou, Q.W. Yang, X.R. Duan, Yong Liu, and HL-2A Team. Bayesian soft x-ray tomography and MHD mode analysis on HL-2A. *Nuclear Fusion*, 2016.
- [14] E. J. Strait. Magnetic diagnostic system of the DIII-D tokamak. *Review of Scientific Instruments*, 2006.
- [15] Teddy Craciunescu, Emmanuele Peluso, Andrea Murari, and Michela Gelfusa. Maximum likelihood bolometric tomography for the determination of the uncertainties in the radiation emission on JET TOKAMAK. *Review of Scientific Instruments*, 2018.
- [16] Diogo R. Ferreira, Pedro J. Carvalho, and Horácio Fernandes. Full-pulse tomographic reconstruction with deep neural networks. *Fusion Science and Technology*, 2018.